RSC Advances

RSC Advances

Volume 1 | Number 1 | Jan 2013 | Pages 1–100

www.rsc.org/advances

ROYAL SOCIETY OF CHEMISTRY

ROYAL SOCIETY OF CHEMISTRY

www.rsc.org/advances

RSC Advances

Paper

Fabrication of highly visible-light-responsive ZnFe₂O₄/TiO₂ heterostructures for the enhanced photocatalytic degradation of organic dyes

Thanh Binh Nguyen[a] and Ruey-an Doong[a, b*]

In this study, a novel visible-light-sensitive ZnFe₂O₄-TiO₂ photocatalyst by coupling 0.2 – 2 wt% narrow bangap material of p-type ZnFe₂O₄ with n-type anatase TiO₂ has been fabricated for the enhanced photocatalytic degradation of organic dyes under 465 nm visible light irradiation. The transmission electron microscopy (TEM) and high resolution TEM confirm that ZnFe₂O₄ and TiO₂ are intimately linked with the average particles size of 8 – 9 nm, leading to the decrease in hole-electron recombination rate as well as the enhanced photocatalytic activity of ZnFe₂O₄-TiO₂ heterostructures under visible light irradiation. The optimized 1 wt% ZnFe₂O₄ not only significantly extends the absorption edge of TiO₂-based heterostructures to the visible light region but can also retain the stable photodegradation efficiency of > 99% for at least 5 cycles. In addition, the photocatalytic activity of ZnFe₂O₄-TiO₂ toward dyes decomposition follows the order cationic rhodamine B > neutral methyl red > anionic methyl orange. Our results clearly demonstrate that the coupling of low loading mass of ZnFe₂O₄ with anatase TiO₂ is a reliable green technology approach to prepare the visible-light-responsive heterostructure photocatalysts with a great potential application for decomposition of organic dyes and other emerging pollutants in water and wastewater treatments.

1. Introduction

The searching and development of excellent semiconductor photocatalysts such as titanium dioxide (TiO₂), zinc oxide (ZnO) and tungsten oxide (WO₃) for water purification and wastewater treatment have recently been attracted tremendous attention.[1] Among the photocatalytic materials used, TiO₂ nanoparticles have been regarded as the excellent photocatalysts because of their high photoreactivity, good photostability, non-toxicity and environmental friendliness.[2] Nevertheless, TiO₂ has a wide bandgap of 3.0 – 3.2 eV and the implementation of pure TiO₂ in practically photocatalytic application is still seriously limited in visible light region, which occupies around 45% of the total sunlight spectrum.[3] Another limitation of TiO₂ photocatalysts is the rapid recombination of electrons and holes. Therefore, it is urgently needed to develop a novel visible-light-responsive TiO₂ based photocatalyst for

environmental applications.

Several methods including doping and surface modification have been attempted to extend the absorption wavelength of TiO₂ to the visible light region.[4-9] Several metal and non-metal ions such as Cu, Ag, Au, Fe, N, C, S and F in the concentration range of 0.5 – 10 wt% have been added as the dopants for the fabrication of visible-light-driven TiO₂ based photocatalysts for effective degradation of organic pollutants and dyes.[10-17] In addition, the combination of TiO₂ with other narrow bandgap semiconductors such as ZnS, RuO₂, CdS and WO₃ has emerged as an important strategy to reduce the bandgap by introducing energy levels between the conduction (CB) and valence bands (VB),[18-21] thus allowing TiO₂ to be active under visible light irradiation. Over the past decades, heterostructures such as ZnO/TiO₂,[22,23] CdS/TiO₂[24, 25] and CuO/TiO₂ nanorods[26, 27] have been developed for the degradation of organic pollutants and water splitting under UV-visible light irradiation. Such nanocomposite structures also favor the enhancement of photoinduced electron-hole separation, and subsequently lead to the acceleration of photodegradation efficiency and rate of pollutants.

A particular interest in the development of visible-light-responsive photocatalysts is the synthesis of nanocrystalline spinel ferrite. Several ferrites including NiFe₂O₄, ZnFe₂O₄ and CuFe₂O₄ have been reported to possess excellent photocatalytic activity for the removal of inorganic contaminants,[28] antimicrobial activity[29, 30]

[a.] *Department of Biomedical Engineering and Environmental Sciences, National Tsing Hua University, Hsinchu, 30013, Taiwan.*

[b.] *Institute of Environmental Engineering, National Chiao Tung University, Hsinchu, 30010, Taiwan. E-mail: radoong@nctu.edu.tw*

†Electronic Supplementary Information (ESI) available: SEM images, particle size distribution, surface area, pore size distribution, EPMA images and Tauc plots of ZnFe₂O₄-TiO₂; Adsorption of rhodamine B by ZnFe₂O₄-TiO₂; Zeta potential of ZnFe₂O₄-TiO₂; Change in absorption spectra of rhodamine B after visible light irradiation; photodegradation of organic dye by pure ZnFe₂O₄; PL spectra of 2-hydroxy terephthalic acid. See DOI: 10.1039/x0xx00000x

ARTICLE

Journal Name

and organic dyes.[31, 32] Moreover, the spinel crystal structure of ferrites offers the available extra catalytic sites by virtue of the crystal lattices to enhance the photodegradation efficiency of pollutants.[33, 34] In particular, the spinel $ZnFe_2O_4$, a magnetic material with narrow bandgap of 1.9 eV, has been used for a wide variety of applications including water splitting, dye sensitized solar cell and photodegradation.[34-36] However, the low VB potential and poor photoelectric conversion efficiency makes $ZnFe_2O_4$ an inferior photocatalyst toward pollutants degradation.[37, 38] Previous studies have shown that the coupling of $ZnFe_2O_4$ with optoelectronic materials such as TiO_2, ZnO and graphene can form a new type of nanocomposite with good photocatalytic activity and separation property.[39-46] It is noteworthy that $ZnFe_2O_4$ is a p-type visible-light-driven semiconductor while anatase TiO_2 is a well-known n-type semiconductor with indirect bandgap and long electron-hole life time.[47, 48] It gives a great impetus to fabricate a novel visible-light-responsive heterostructure photocatalyst by combining $ZnFe_2O_4$ with anatase TiO_2. However, the fabrication of $ZnFe_2O_4$-TiO_2 nanocomposites by coupling trace amounts of $ZnFe_2O_4$ with pure anatase TiO_2 has received less attention. In addition, the added amount of $ZnFe_2O_4$ on the photocatalytic activity of heterostructure photocatalysts remains unclear.

Herein, a novel $ZnFe_2O_4$-TiO_2 nanocomposite has been fabricated for the enhanced visible-light-responsive photodegradation of organic dyes including neutral rhodamine B (RhB), cationic methyl red (MR) and anionic methyl orange (MO) in the presence of 465 nm visible light. Non-aqueous hydrothermal method was used to fabricate nanoscale $ZnFe_2O_4$ particles at low mass loadings of 0.2 – 2 wt% and then coupled with pure anatase ST01 TiO_2 for optimization. The morphology and surface characterization confirm that $ZnFe_2O_4$ is well distributed with TiO_2. $ZnFe_2O_4$ in the nanocomposites can be excited by visible light and then the anatase TiO_2 serves as the charge carrier to participate the surface reaction, resulting in the enhancement of photocatalytic activity of $ZnFe_2O_4$-TiO_2 heterostructures toward dye decomposition. To the best of our knowledge, this is the first report to the optimization of mass ratio of zinc ferrite for the enhanced photocatalytic degradation efficiency of organic dyes by TiO_2 based nanomaterials under visible light irradiation. In addition, the excellent reusability of nanocomposites indicates that $ZnFe_2O_4$-TiO_2 has a wide variety of potential of utilizing visible light in environmental and energy applications.

2. Materials and methods

2.1. Synthesis of zinc ferrite ($ZnFe_2O_4$)

$ZnFe_2O_4$ nanoparticles were first synthesized by non-aqueous hydrothermal method. Briefly, 10 mmol of NaOH was dissolved in 2 mL of bidistilled deionized water (Millipore Co, 18.3 MΩ cm) in an autoclave tube with a capacity of 40 mL. After the addition of 10 mL of 1-pentanol ($C_5H_{12}O$) under vigorous stirring, 0.5 mmol of oleic acid ($C_{18}H_{34}O_2$) and 0.5 mmol oleylamine ($C_{18}H_{37}N$), which served as capping agents, were introduced into the solutions. A total of 2

mmol of iron nitrate ($Fe(NO_3)_3.9H_2O$) and 1 mmol of zinc nitrate ($Zn(NO_3)_2.6H_2O$) was dissolved in 14 mL of bidistilled deionized water and then was poured into the above solutions. After well mixing for 1 h, the mixture was heated to 180 °C for 16 h, cooled down to room temperature, and then the $ZnFe_2O_4$ nanoparticles were magnetically harvested from the liquid phase by using permanent magnet. The nanoparticles were washed with *n*-hexane/ethanol (3/1, v/v) mixture three times to remove excess capping agent on the surface. Finally, $ZnFe_2O_4$ nanoparticles were re-dispersed in *n*-hexane, transferred to the watch glass, and dried in a vacuum oven at 60 ºC for 6 h.

2.2. Synthesis of $ZnFe_2O_4$-TiO_2 nanocomposites

The $ZnFe_2O_4$-TiO_2 nanocomposite photocatalysts were synthesized by mixing 80 mg of ST01 TiO_2 (Ishihara Sangyo Ltd.) with various mass loadings of $ZnFe_2O_4$ at 0.2 – 2 wt% in 20 mL of octanol ($C_8H_{18}O$) and then sonicated for 1 h. The mixture was transferred into a 40 mL autoclave tube and heated to 240 ºC for 2 h. The mixture was again cooled down to room temperature and then centrifuged at 11,000 rpm for 15 min to harvest the nanocomposites. Similar to the preparation procedure of $ZnFe_2O_4$, the $ZnFe_2O_4$-TiO_2 precipitates were washed with mixture of *n*-hexane/ethanol three times, and dried in a vacuum oven at 60 ºC for 6 h.

2.3. Characterization

The surface morphology of as-synthesized $ZnFe_2O_4$-TiO_2 was examined by using scanning electronic microscopy (SEM) (Hitachi S-4800) with an acceleration electron voltage of 15 kV. The transmission electron microscopy (TEM) (Hitachi H-7100 TEM) and high resolution TEM (HRTEM) (FEI tecnai G2) at 200 and 300 kV, respectively, were used to determine the dimension and morphology of $ZnFe_2O_4$-TiO_2. The distribution of elements was determined by an electron probe X-ray microanalyzer (JEOL JXA-8200) with an accelerating voltage and beam current 20 kV and 20 nA. The Brunauer-Emmett-Teller (BET) specific surface area and pore size distribution were determined by nitrogen adsorption and desorption at 77 K using a surface area and porosimetry system (ASAP 2020, Micromeritics). The crystallinity of $ZnFe_2O_4$-TiO_2 nanocomposites were identified by a Bruker NEW D8 ADVANCE X-ray diffractometer (XRD) with a Lynxeye high-speed strip detector and Ni-filtered Cu Kα radiation (λ = 1.5405Å) operating at a generator voltage and an emission current of 40 kV and 40 mA, respectively. The XRD patterns were recorded over the 2θ range of 20-80º at a sampling step width 0.05º (step time = 0.5 s). The X-ray photoelectron spectroscopy (XPS) measurements were performed by an ESCA PHI 1600 photoelectron spectrometer (Physical Electronics, Eden Prairie, MN) using Al Kα X-ray source at 1486.6 ± 0.2 eV. The optical spectra was examined by using a Hitachi U-4100 UV–vis spectrophotometer in the wavelength range of 200 – 800 nm equipped with the integrating sphere accessory for diffuse reflectance spectra. Photoluminescence (PL) spectra were recorded on a Hitachi F-7000 fluorescence spectrometer with a 150 W
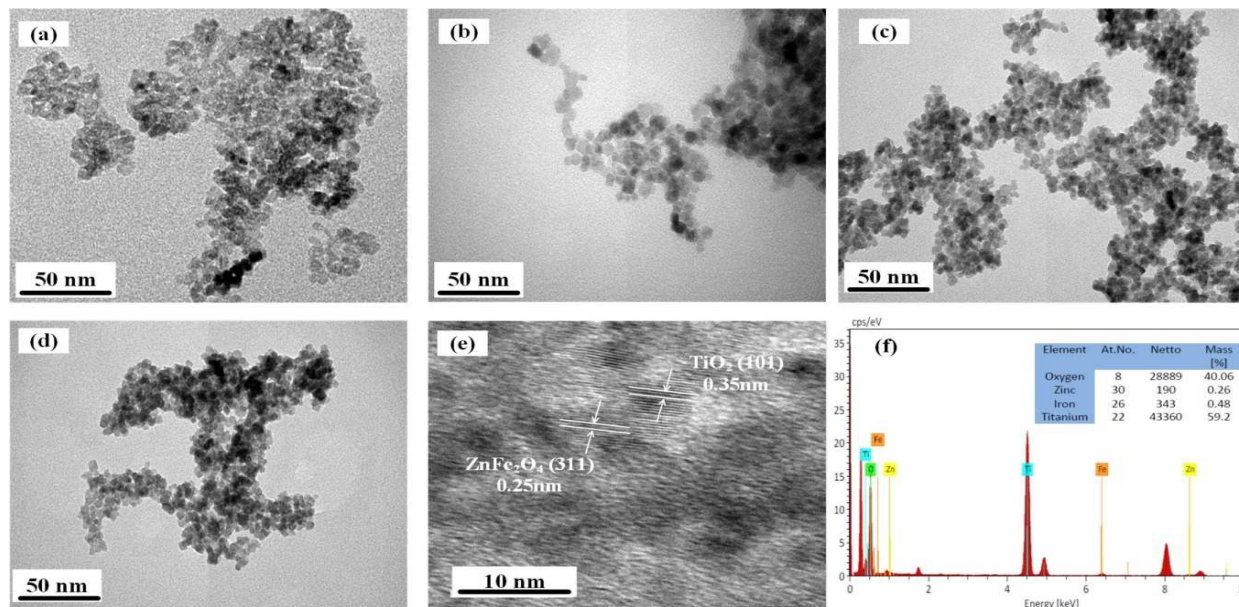
RSC Advances

Paper

Fig. 1. The TEM images of $ZnFe_2O_4$-TiO_2 nanocomposites at (a) 0.5, (b) 1, (c) 1.5 and (d) 2 wt% $ZnFe_2O_4$ nanoparticles. (E) and (f) are HRTEM image and EDS spectrum of 1 wt% $ZnFe_2O_4$-TiO_2 nanocomposites, respectively.

xenon lamp as the excitation source.

The photocurrent was determined by using a three-electrode system connected to an electrochemical work station (Autolab PGSTAT 302N) in the presence of 0.2 M $Na_2S_2O_4$ as the electrolytes. $ZnFe_2O_4$-TiO_2/FTO electrode was used as the working electrode, and the Ag/AgCl electrode and platinum wire were used as the reference and counter electrodes, respectively. The transient photocurrent of pure $ZnFe_2O_4$, commercial TiO_2 and $ZnFe_2O_4$-TiO_2 nanocomposites were measured at an applied potential of 1 V under visible light irradiation. The surface charge (zeta potential) of $ZnFe_2O_4$-TiO_2 nanocomposites was determined by using ZetaSizer Nano ZS (Malvern Instruments Inc., UK).

2.4. Photodegradation of organic dyes by $ZnFe_2O_4$-TiO_2

The visible-light-responsive activity of $ZnFe_2O_4$-TiO_2 was examined by using RhB, MR and MO as the target compounds in a hollow cylindrical photoreactor surrounded by eight 8W visible lamps (λ = 465±40 nm). In each experiment, the as-synthesized photocatalysts as well as commercial TiO_2 nanoparticles were added into the 20 mL of 10 mg/L dye solutions to get the final concentration of 1 g/L. Prior to the photocatalytic reaction, the mixtures were well-mixed under vigorous stirring conditions in the dark for 60 min and at 25 ºC to avoid the interference of adsorption during the photocatalytic reactions. After the adsorption equilibrium, the visible light was switched on for photodegradation and the change in dye concentration in supernatants was optically monitored by UV-Vis spectrophotometer after the removal of photocatalysts by centrifugation at 14,000 rpm for 5 min.

3. Results and discussion

3.1 Characterization of $ZnFe_2O_4$-TiO_2 nanocomposites

In this study, various amounts of $ZnFe_2O_4$ were added as dopants to improve the visible-light-responsive activity of TiO_2. Fig. 1 shows the TEM images of $ZnFe_2O_4$-TiO_2 nanocomposites with various $ZnFe_2O_4$ amounts of 0 – 2 wt%. The TEM image shows that the $ZnFe_2O_4$-TiO_2 nanocomposites are regular-shaped crystallite (Fig. 1(a)-(d)). However, the $ZnFe_2O_4$-TiO_2 nanoparticles agglomerate to some extents, presumably attributed to the magnetic property of $ZnFe_2O_4$ particles. The SEM images illustrated in Fig. S1 (†ESI) clearly shows the slight increase in particle size of $ZnFe_2O_4$-TiO_2 nanocomposites when the loading amount of $ZnFe_2O_4$ increases from 0.5 to 2 wt%. The histogram shown in Fig. S2 (†ESI) indicates that the particle sizes of $ZnFe_2O_4$-TiO_2 nanocomposites at 0.2 – 2 wt% $ZnFe_2O_4$ are in the range of 7 – 11 nm. However, the mean particle size increases slightly from 7.5 nm at 0.2 wt% to 8.7 nm at 2 wt%, which is in good agreement with the results obtained from the SEM images.

ARTICLE

Journal Name

The HRTEM image of 1 wt% $ZnFe_2O_4$-TiO_2 nanocomposites shows two distinct lattices with d-spacings of 0.25 and 0.35 nm, which correspond to the (311) reflection of $ZnFe_2O_4$ and (101) reflection of anatase TiO_2, respectively (Fig. 1(e)). It is clearly that both $ZnFe_2O_4$ and TiO_2 are nanosized particles with average particle size of 8 nm. The EDS spectrum indicates the existence of Ti, Zn and Fe elements and that the weight ratio is 0.26 wt% for Zn and 0.48 wt% for Fe (Fig. 1(f)). The Fe/Zn molar ratio of 2.1 clearly indicates the formation of $ZnFe_2O_4$. In addition, the $ZnFe_2O_4$ nanoparticles are tightly linked with TiO_2 nanoparticles. Since both TiO_2 and $ZnFe_2O_4$ have similar particle sizes and are initially contacted, the $ZnFe_2O_4$-TiO_2 nanocomposites may be favorable for the charge transfer between $ZnFe_2O_4$ and TiO_2, and results in the promotion of electron–hole pairs separation as well as the enhancement of photocatalytic performance.

The elemental species in $ZnFe_2O_4$-TiO_2 nanomaterials were further identified by EPMA. Fig. S3 (†ESI) shows the elemental images of Ti, Zn, Fe and O in the 1 wt% $ZnFe_2O_4$-TiO_2 nanocomposites. The uniformly distribution of Ti and O atoms indicates that TiO_2 nanoparticles are well distributed. In addition, the distribution of Zn and Fe are quite homogeneous with low intensity when compares with those of Ti and O atoms, presumably attributed to the low loading amount of $ZnFe_2O_4$.

The N_2 adsorption-desorption isotherms of $ZnFe_2O_4$ and $ZnFe_2O_4$-TiO_2 nanocomposites with 0.2 – 2wt% $ZnFe_2O_4$ exhibited similar type IV isotherms with hysteresis loop in the relative pressure P/P_0 within the range of 0.7 – 0.95 (Fig. S4a, †ESI), indicating the presence of mesopores in the nanocomposites. The specific surface area of $ZnFe_2O_4$-TiO_2 increased from 123 m^2/g at 0.2 wt% $ZnFe_2O_4$ to 178 m^2/g at 1.5 wt% $ZnFe_2O_4$, and then slightly decreased to 164 m^2/g at 2 wt% $ZnFe_2O_4$. It is noteworthy that the specific surface area of pure $ZnFe_2O_4$ was 113 m^2/g, showing that the combination of TiO_2 with $ZnFe_2O_4$ can increase the specific surface area. In addition, the pore size distribution of pure $ZnFe_2O_4$ was in the range 2–18 nm with average pore diameter of 12 nm (Fig.
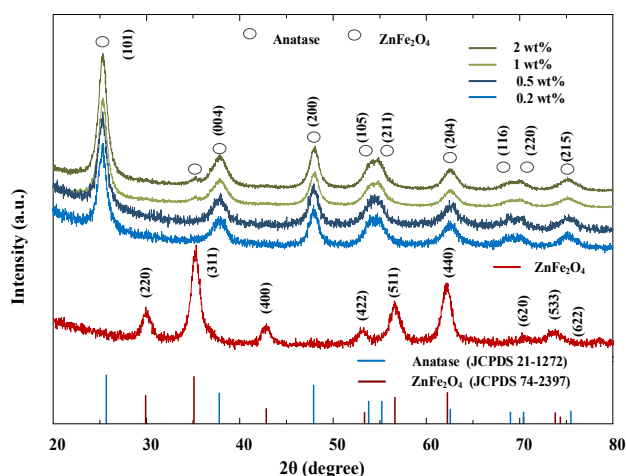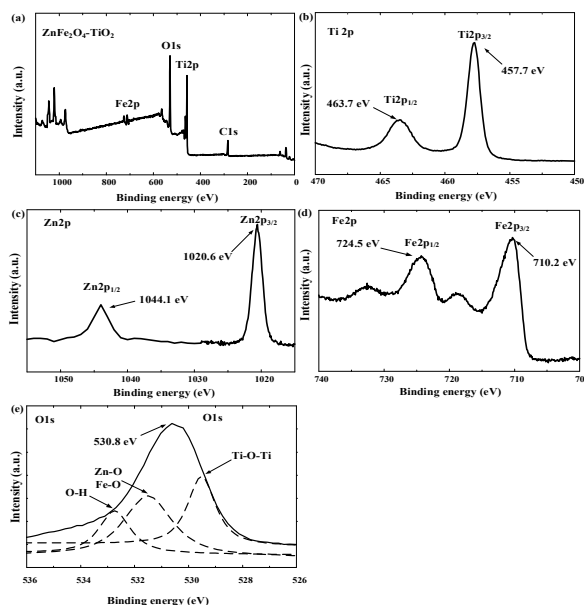

Fig. 3. The (a) full survey XPS spectra and (b) Ti 2p, (c) Fe 2p (d) Zn 2p and (e) O 1s peak of 1 wt% $ZnFe_2O_4$-TiO_2 nanocomposites.

S4b, †ESI). The $ZnFe_2O_4$-TiO_2 nanocomposites also showed the major pore size distribution in the range of 4–15 nm. However, another small pore size distribution ranging between < 1.7–4 nm was also observed for 0.5–2 wt% $ZnFe_2O_4$, clearly showing that the increase in specific surface area of $ZnFe_2O_4$-TiO_2 nanocomposites is mainly attributed to the increase in mesopore.

The crystallinity of pure $ZnFe_2O_4$, TiO_2 and various $ZnFe_2O_4$ loadings of $ZnFe_2O_4$-TiO_2 nanocomposites were further identified. As shown in Fig. 2, several diffraction peaks centered at 29.89°, 35.24°, 42.97°, 53.16°, 56.79° and 62.28° 2θ, which are characteristic peaks of (220), (311), (400), (422), (511) and (440) orientations of $ZnFe_2O_4$, respectively (JCPDS 74-2397). The average grain size of $ZnFe_2O_4$, calculated from Scherrer equation, is around 8 nm. In addition, the XRD patterns of $ZnFe_2O_4$-TiO_2 nanocomposites show the major peaks of anatase phase of TiO_2 at 25.28°, 48.37°, 53.88°, 55.29°, 62.73°, 68.99°, 70.17°, and 75.37° 2θ (JCPDS 21-1272) and a small peak of $ZnFe_2O_4$ at 35.24° 2θ, indicating that the composites can retain the crystallinity of both nanoparticles. It is noteworthy that only few peaks of $ZnFe_2O_4$ in XRD patterns are identified, presumably attributed to the low loading amount of $ZnFe_2O_4$ onto TiO_2. In addition, no rutile peak of TiO_2 is observed in all the as-synthesized $ZnFe_2O_4$-TiO_2 nanocomposites, showing that the crystallinity of anatase phase of ST01 TiO_2 can be retained during the preparation procedures.

The XPS spectra were further characterized to understand the chemical states of elements in $ZnFe_2O_4$-TiO_2 nanocomposites. The survey scan illustrated in Fig. 3a shows the coexistence of Zn 2p, Fe 2p, Ti 2p and O 1s elements in the as-synthesized $ZnFe_2O_4$-TiO_2 nanocomposites. In addition, the existence of C 1s at 285 eV is ascribed to the adventitious carbons from the ambient environments. The high resolution XPS spectrum of Ti 2p shows two

Fig. 2. The XRD patterns of pure $ZnFe_2O_4$, TiO_2 and $ZnFe_2O_4$ -TiO_2 nanocomposites with various mass loadings of $ZnFe_2O_4$ ranging from 0.5 to 2 wt%.

Journal Name

ARTICLE

peaks located at 463.7 eV and 457.7 eV, which can be assigned as the Ti^{4+} peak of anatase TiO_2 (Fig. 3b).[39] The peaks at 1020.6 and 1044.1 eV shown in Fig. 3c are attributed to Zn^{2+} at tetrahedral sites. Peaks of Fe 2p at 710.2 and 724.5 eV are the typical $2p_{3/2}$ and $2p_{1/2}$ of iron oxide, respectively. In addition, peaks at 719.2 and 732.8 eV are the satellite peaks of iron oxides, which confirm the existence of Fe^{3+}.[49] The deconvolution of high-resolution XPS spectrum of O 1s region shows the typical peaks of metal-oxygen bonds of TiO_2 and $ZnFe_2O_4$ (Fig. 3d),[49] clearly indicating the coexistence and interaction of $ZnFe_2O_4$ and TiO_2 in the composites.

The UV-visible and PL spectra of $ZnFe_2O_4$-TiO_2 nanocomposites were determined to understand the optical properties of the nanocomposites. Fig. 4a presents the absorbance of $ZnFe_2O_4$-TiO_2 nanocomposites with various loading amounts of $ZnFe_2O_4$ ranging from 0.2 to 2 wt%. It is clear that pure $ZnFe_2O_4$ shows high absorption intensity in the visible light region. The absorption edge of pure ST01 TiO_2 starts to increase at 380 nm, which is coincident with the reported result of anatase TiO_2.[50] Addition of $ZnFe_2O_4$ red-shifts the absorbance edge of $ZnFe_2O_4$-TiO_2 nanocomposites to the long wavelength region when the added amount of $ZnFe_2O_4$ increases from 0.2 to 2 wt%. Since the TiO_2 is an indirect band gap semiconductor, the Tauc plot can be used to calculate the bandgap of $ZnFe_2O_4$-TiO_2 nanocomposites.[51] As shown in Fig. S4 (†ESI), the bandgap of pure ST01 TiO_2 is 3.18 eV, and then decreases to 2.88 – 2.56 eV when the added amounts of $ZnFe_2O_4$ increases from 0.2 to 2 wt%. It is noteworthy that the narrow band gap of $ZnFe_2O_4$ at 1.9 eV may induce the lattice defects of anatase TiO_2 under UV-visible light irradiation, which can serve as the center of bound excitons to enhance the photoactivity of $ZnFe_2O_4$-TiO_2 nanocomposites.[52]

Fig. 4(b) shows the PL spectra of pure TiO_2 and $ZnFe_2O_4$-TiO_2 nanocomposites at various loading amounts of $ZnFe_2O_4$ in the wavelength range of 300-500 nm after the excitation at 285 nm. The PL spectra of all the $ZnFe_2O_4$-TiO_2 nanocomposites show the major peak at 315 nm, which is mainly attributed to the recombination of holes and electrons in the valence and conduction bands, respectively. The emission intensity at 315 nm decreases with the increase in $ZnFe_2O_4$ loading from 0 to 1 wt%, and then again increases slightly at 2 wt% $ZnFe_2O_4$. It is noteworthy that the PL spectra can be used to understand the behaviors of electron-hole pairs on trapping, immigration, and transfer properties.[53, 54] Since the emission signal at 315 nm originates from the recombination of excited electrons and holes, the decrease in fluorescence intensity is highly relevant to the low recombination rate of holes and electrons. This indicates that 1 wt% $ZnFe_2O_4$-TiO_2 nanocomposites may exhibit superior photocatalytic activity to the other nanocomposites toward pollutant degradation. In addition, the separation efficiency of photo-induced electron-hole pairs can be compared by the transient photocurrent response in several 100s on-off intermittent irradiation cycles. As shown in Fig. 4(c), pure $ZnFe_2O_4$ and commercial TiO_2 nanoparticles including P25 and ST01 TiO2 showed low transient photocurrent and the produced photocurrent current followed the order $ZnFe_2O_4$ < ST01 TiO_2 < P25 TiO_2, which is highly related to their bandgaps. On the contrary, 1 wt% $ZnFe_2O_4$-TiO_2 nanocomposites showed excellent

photoresponse than the other photocatalysts and the photocurrent density can be maintained at 5.9 $\mu A/cm^2$ during the 4 cycles. This result clearly indicates that the 1 wt% $ZnFe_2O_4$-TiO_2 nanocomposites can exhibit long lifetime of photoinduced carriers, and subsequently results in the high photocatalytic activity toward organic dye degradation.
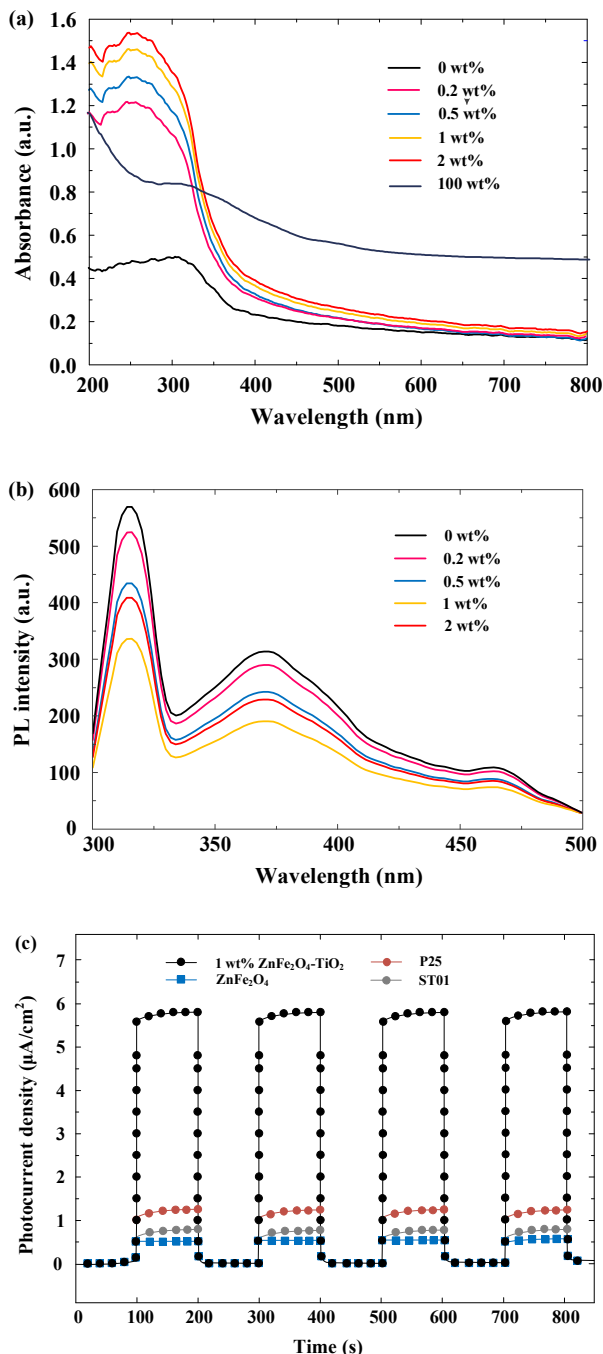

Fig. 4. The (a) UV-Vis diffuse reflectance, (b) photoluminescence spectra of $ZnFe_2O_4$-TiO_2 nanocomposites at various mass loadings of $ZnFe_2O_4$ ranging from 0 to 2 wt%. and (c) transient photocurrent response of various materials.

ARTICLE

Journal Name

3.2. The visible-light-responsive activity of ZnFe$_2$O$_4$-TiO$_2$ toward organic dye degradation

The visible-light-sensitive activity of ZnFe$_2$O$_4$-TiO$_2$ nanocomposites was first evaluated by using RhB as the target compound under 465 nm visible light irradiation. As shown in Fig. 5(a), only 1.4 % of RhB concentration is photodegraded after 60 min of visible light irradiation in the absence of ZnFe$_2$O$_4$-TiO$_2$ photocatalyst (direct photolysis). The pure anatase ST01 TiO$_2$ shows little photocatalytic activity toward RhB degradation under 465 nm visible light irradiation, presumably attributed to their wide bandgap of 3.18 eV. The addition of ZnFe$_2$O$_4$ exhibits a significant impact on the photodegradation efficiency and rate of RhB and 92.6% of the initial RhB is photodegraded by 0.2 wt% ZnFe$_2$O$_4$-TiO$_2$. The removal efficiency of RhB increases upon increasing the loading amounts of ZnFe$_2$O$_4$ from 0.5 to 1 wt% and then slightly decreases when further increases the ZnFe$_2$O$_4$ amount to 2 wt%. Addition of 1 wt% ZnFe$_2$O$_4$-TiO$_2$ shows the superior photocatalytic activity toward RhB degradation when compares to other added amounts of ZnFe$_2$O$_4$, which is in good agreement with the optical data obtained from the PL spectra.

It is noteworthy that the equilibrium of 60 min between organic dye and various loading amounts of ZnFe$_2$O$_4$-TiO$_2$ causes a 30 – 48% decrease in RhB concentration prior to the photodegradation, showing that adsorption is a possible mechanism for RhB removal. To further understand the adsorption effect on the removal of RhB by TiO$_2$-based nanomaterials, adsorption of RhB by the commercial TiO$_2$ and 1 wt% ZnFe$_2$O$_4$-TiO$_2$ was performed in the dark. As shown in Fig. S5 (†ESI), less than 5% of RhB concentration are adsorbed in solutions containing commercial TiO$_2$ products including Degussa P25 and ST01 TiO$_2$ after 120 min of adsorption in the dark. In the presence of 1 wt% ZnFe$_2$O$_4$-TiO$_2$, however, the concentration of RhB decreases with time during the first 60 min and a total of 48% of RhB is adsorbed by 1 wt% ZnFe$_2$O$_4$-TiO$_2$ after 120 min of incubation. The adsorption of RhB is mainly attributed to the fact that ZnFe$_2$O$_4$-TiO$_2$ is fabricated by using non-aqueous hydrothermal method and would contain some organic residues onto the surface after phase transfer. In addition, the pH$_{IEP}$ of 1 wt% ZnFe$_2$O$_4$-TiO$_2$ is 6.7 (Fig. S6, †ESI), which means that the ZnFe$_2$O$_4$-TiO$_2$ is negatively charged at pH 7. Therefore, the cationic RhB would adsorb onto the surface of ZnFe$_2$O$_4$-TiO$_2$. These results clearly indicate that the adsorption can be equilibrated within 60 min prior to the photodegradation and has little influence on the photodegradation efficiency and rate of RhB.
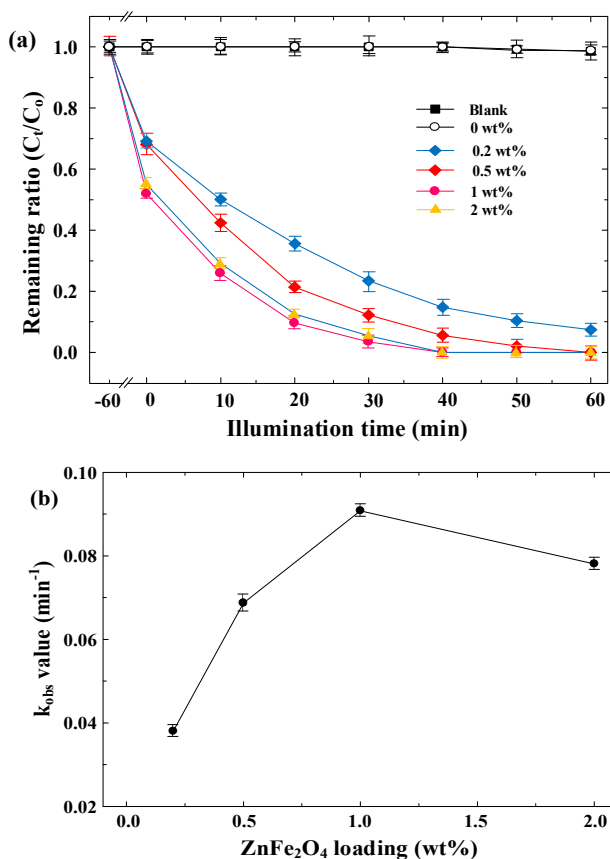

Fig. 5. The (a) photodegradation of rhodamine B (RhB) and (b) pseudo-first-order rate constants (k$_{obs}$) for RhB degradation by various loading amounts of ZnFe$_2$O$_4$–TiO$_2$ under 465 nm visible light irradiation.
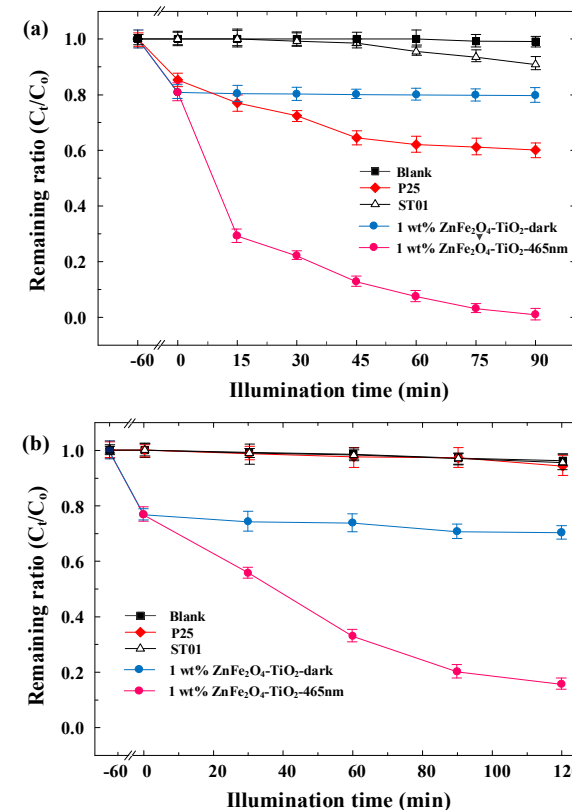

Fig. 6. The photodegradation of (a) neutral methyl red (MR), and (b) anionic methyl orange (MO) in the presence of 1 wt% ZnFe$_2$O$_4$–TiO$_2$ under visible light irradiation.

Journal Name

ARTICLE

The photocatalytic degradation of organics by TiO_2-based nanomaterials usually obeys the pseudo-first-order kinetics.[55] In this study, the decrease in RhB concentration follows the adsorption first and then undergoes the photodegradation. After subtracting the adsorption part, the photocatalytic degradation of RhB follows the pseudo-first-order kinetics and the rate constants (k) for RhB photodegradation by 0.2, 0.5, 1, and 2 wt% $ZnFe_2O_4$-TiO_2 are 0.038 (r^2 = 0.998), 0.069 (r^2 = 0.986), 0.091 (r^2 = 0.993) and 0.078 (r^2 = 0.996) min^{-1}, respectively (Fig. 5b). The UV-visible spectra of aqueous RhB solutions in the presence of 1 wt% $ZnFe_2O_4$-TiO_2 under 465 nm visible light irradiation show that the intensity of absorption peak at 554 nm decreases rapidly with time, indicating the excellent visible-light-responsive activity of $ZnFe_2O_4$-TiO_2 nanocomposites (Fig. S6, †ESI). It is noteworthy that the maximum absorption peak blue-shifts from 554 to 498 nm after 60 min of visible light irradiation. A previous study has investigated the decomposition of RhB by N-doped TiO_2 based nanoparticles and found that the de-ethylated intermediates could cause the shift in absorption band during the photodegradation,[56] which is in good agreement with the results obtained in this study.

To further understand the photocatalytic activity of $ZnFe_2O_4$–TiO_2 toward different types of organic dyes, photodegradation experiments were performed by selecting methyl red (MR) and methyl orange (MO) as the neutral and anionic dyes, respectively. In addition, 1 wt% $ZnFe_2O_4$-TiO_2 was selected as the photocatalyst for further experiments. Fig. 6 shows the photocatalytic degradation efficiency and rate of MR and MO by 1 wt% $ZnFe_2O_4$-TiO_2 under visible light irradiation. The photodegradation efficiencies of MR by commercial ST-01 and Degussa P-25 TiO_2 are 10% and 40%, respectively (Fig. 6a). In addition, pure $ZnFe_2O_4$ only shows slight effect on photodegradation on the three organic dyes under the same experimental conditions (Fig. S9, †ESI). Addition of 1 wt% $ZnFe_2O_4$–TiO_2 enhances the photocatalytic degradation efficiency of MR and a nearly complete photodegradation is observed within 90 min of irradiation (Fig. 6a). However, only 82% of MO is photodegraded by $ZnFe_2O_4$–TiO_2 after 90 min of irradiation (Fig. 6b). It is noteworthy that 20% of MR and 22% of MO are adsorbed by $ZnFe_2O_4$–TiO_2 in the dark. The less adsorbed amounts of MR and MO compared with that of RhB is mainly due to the negatively charged surface of $ZnFe_2O_4$–TiO_2. In addition, the molecular structure of organic dyes shows a great impact on photocatalytic activity of $ZnFe_2O_4$–TiO_2 and the k_{obs} for dye photodegradation is 0.0445 min^{-1} for MR and 0.0136 min^{-1} for MO. This result clearly indicates that photodegradation rate of organic dyes by $ZnFe_2O_4$-TiO_2 follows the order RhB > MR > MO (Fig. 7c). It is noteworthy that the photocatalytic degradation of organic chemicals is a surface-mediated reaction,[7] and adsorption of organic dyes onto the surface of $ZnFe_2O_4$-TiO_2 is the first step for photodegradation. The cationic RhB can be easily adsorbed onto the negative charged $ZnFe_2O_4$-TiO_2 and show excellent photocatalytic efficiency and rate than those of neutral MR and anionic MO. Therefore, RhB is selected for further experiments because of the excellent photocatalytic degradation efficiency and rate.
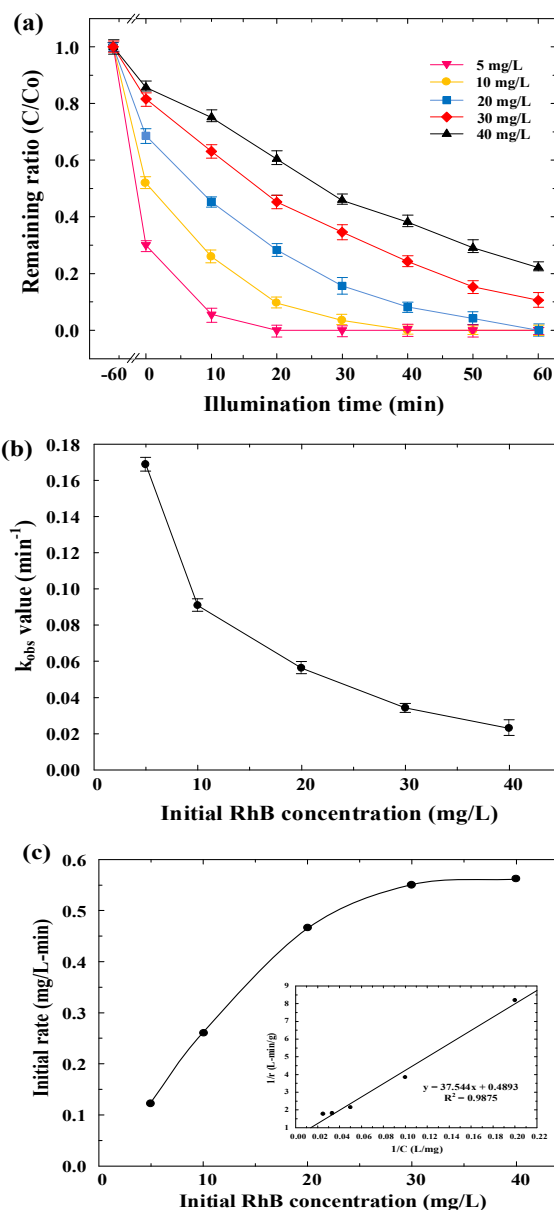

Fig. 7. The (a) photocatalytic degradation of RhB at various initial concentrations, (b) k_{obs} for RhB photodegradation and (c) initial rate of RhB as a function of initial RhB concentrations by 1 wt% $ZnFe_2O_4$–TiO_2 under visible light irradiation.

3.3. Effect of RhB concentration on photodegradation

The photodegradation of various initial concentrations of RhB was further examined. Fig. 7 shows the photodegradation of various initial concentrations of RhB by 1 wt% $ZnFe_2O_4$–TiO_2 under 465 nm visible light irradiation. It is evident that the photodegradation efficiency of RhB decreases with the increase in initial RhB concentrations ranging from 5 to 40 mg/L. As shown in Fig. 7a, a nearly complete photodegradation of 5 mg/L RhB by 1 wt% $ZnFe_2O_4$-TiO_2 is observed after 60 min of irradiation. However, only 79% of the original RhB is photodecomposed when RhB

ARTICLE

concentration increases to 40 mg/L. The photodegradation of RhB at various initial concentrations also follows the pseudo-first-order kinetics and the k_{obs} for RhB photodegradation decreases from 0.1687 to 0.0229 min^{-1} when the initial concentration increases from 5 to 40 mg/L (Fig. 7b). The decrease in k_{obs} for RhB photodegradation at high initial concentration is possibly attributed to the inhibition effect of adsorbed RhB molecules on light penetration. It is noteworthy that RhB is a red-colored dye and the increase in RhB concentration would absorb more light. Therefore, the increase in initial RhB concentration decreases the penetration of photons to the photocatalyst surface, resulting in the decrease in the photocatalytic degradation efficiency and rate of RhB.[57]

The limited reactive site onto the ZnFe$_2$O$_4$–TiO$_2$ nanocomposite is another plausible reason for the decreased rate constants. Our previous studies have indicated that the photocatalytic degradation of organic pollutants by photocatalysts obey the surface-mediated processes and the Langmuir-Hinshelwood kinetics can be employed to describe the relationship:[7]

$$r_0 = \frac{dC_R}{dt} = k_r \frac{K_a C_R}{1 + K_a C_R}$$

$$(1)$$

where r_o is the initial rate for RhB photodegradation, C_R is the RhB concentration; k_r is the intrinsic rate constant, and K_a is the Langmuir coefficient of RhB. Fig. 7(c) shows the relationship between the initial rate for RhB photodegradation and the initial RhB concentration. It is clear that the initial rate of RhB photodegradation increases rapidly from 0.12 to 0.545 mg/L-min at initial RhB concentration of 5–30 mg/L and then reaches the plateau of 0.565 mg/L-min at 40 mg/L RhB. A good linear relationship between $1/r_o$ and $1/C_R$ with r^2 of 0.988 is observed (inset of Fig. 7(c)). The K_a and k_r values are calculated to be 0.013 L/mg and 2.043 mg/L-min, respectively, clearly showing that the photodegradation of RhB by ZnFe$_2$O$_4$-TiO$_2$ is a surface-mediated process.

3.4. Reusability of ZnFe$_2$O$_4$-TiO$_2$

The recovery and reusability are also important parameters for evaluation of possible application of photocatalysts. In this study, the photocatalytic reusability of ZnFe$_2$O$_4$–TiO$_2$ was further examined by repeatedly injection of 10 mg/L RhB under visible light irradiation. As shown in Fig. 8, RhB can be rapidly photodegraded by 1 wt% ZnFe$_2$O$_4$–TiO$_2$ within 60 min. After the re-injection of same concentration of RhB into the solutions, ZnFe$_2$O$_4$–TiO$_2$ still exhibit excellent visible-light-responsive activity and can effectively photodegrade RhB to > 99% for at least 5 cycles. The k_{obs} for RhB photodegradation decreases from 0.0908 min^{-1} for the first cycle to 0.0589 min^{-1} at the 5th addition. The decrease in rate constant is mainly attributed to the accumulation of intermediates after photocatalytic degradation of RhB, which is in good agreement with the UV-visible spectra shown in Fig. S7(†ESI).

3.5. Possible reaction mechanism

In this study, ZnFe$_2$O$_4$-TiO$_2$ nanocomposites have shown the excellent photocatalytic activity toward organic dye degradation. It is known that TiO$_2$ is a UV-sensitive photocatalyst and addition of narrow-bandgap material of ZnFe$_2$O$_4$ can enhance the visible-light-responsive property of nanocomposites. As shown in Scheme 1, electrons in the VB of ZnFe$_2$O$_4$ can be photo-excited to CB after the irradiation of visible light, and result in the production of electron-hole pairs. Since the energy position of CB of ZnFe$_2$O$_4$ at -1.54 eV is higher than that of anatase TiO$_2$ (-0.30 eV),[58] the excited electrons in ZnFe$_2$O$_4$ can be easily transferred across the interface of nanocomposites to the CB of anatase TiO$_2$, and leaves holes in the VB of ZnFe$_2$O$_4$. Therefore, the coupling of ZnFe$_2$O$_4$ and TiO$_2$ can effectively reduce the recombination rate of electrons and holes, and subsequently enhances the interfacial charge transfer efficiency. It is noteworthy that the photogenerated holes (h$^+$) in the valence band of ZnFe$_2$O$_4$ cannot react with the surface-absorbed H$_2$O to generate the highly reactive hydroxyl radicals ($^\bullet$OH) because of the lower valence band position (0.38 eV) in comparison with that of water oxidation [E^0 ($^\bullet$OH/OH$^-$) = 2.38 V]. In contrast, electrons in the conduction band of TiO$_2$ at pH 7 is -0.29 V which can provide the sufficient reducing power to generate superoxide anion (O$_2^-\bullet$) and peroxyl (HO$_2\bullet$) radicals [E^0 (O$_2$/O$_2^-\bullet$) = -0.33 V and E^0 (O$_2$/HO$_2\bullet$) = -0.05 V]. The produced oxygen-containing radicals (O$_2^-\bullet$ and HO$_2\bullet$) can further react with electrons and protons to produce hydroxyl radicals ($\bullet$OH), resulting in the enhanced photodegradation efficiency and rate of RhB and other organic dyes under visible light irradiation. It is noteworthy that Z-scheme electron transfer can be occurred when the two narrow-bandgap photocatalysts are excited by visible light. During the Z-scheme electron transfer, the photogenerated electrons in the low CB of photocatalyst I are transferred to the high VB of photocatalyst II through the electron mediator.[59] In this study, only ZnFe$_2$O$_4$ can be excited by 465 nm visible light and then the photogenerated electrons in the CB of ZnFe$_2$O$_4$ transfer to the CB of TiO$_2$. Since there is lacking of electron mediator which can transfer electrons from the CB of TiO$_2$ to the VB of ZnFe$_2$O$_4$, the electron transfer mechanism in this study is more resemble to that of the heterostructured photocatalytic system.
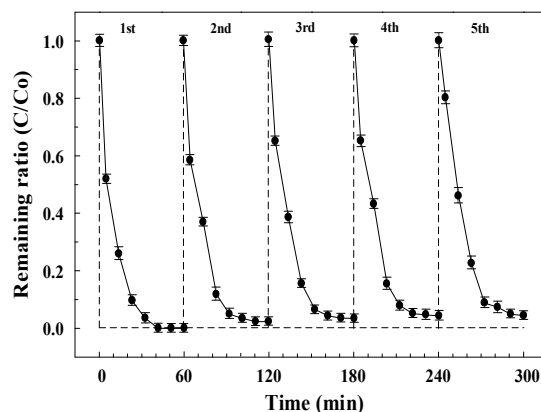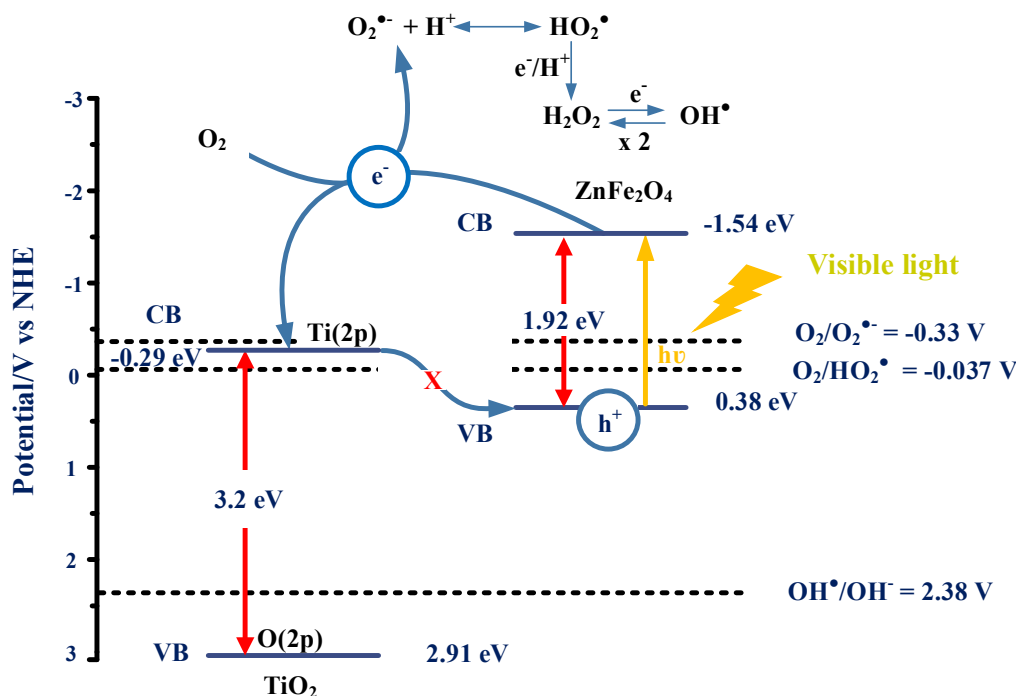
Fig. 8. The photodegradation of rhodamine B (RhB) by the recycled 1 wt% $ZnFe_2O_4$-TiO_2 under 465 nm visible light irradiation.

Scheme 1. The possible photocatalytic mechanism for organic dye degradation by $ZnFe_2O_4$-TiO_2 under visible light irradiation.

To demonstrate the generation of hydroxyl radical ($^\bullet$OH) by visible light irradiation, terephthalic acid (TPA), a fluorescent probe which can readily react with hydroxyl radicals to produce a highly fluorescent product of 2-hydroxy terephthalic acid (TAOH) at 425 nm, was used in the $ZnFe_2O_4$-TiO_2 system under 465 nm visible light irradiation.[60] Fig. S8 (†ESI) shows the change in PL spectra of TAOH after the visible light irradiation of 1 wt% $ZnFe_2O_4$-TiO_2 in the presence of 5×10^{-4} M TPA solutions. It is clear that the PL intensity at 425 nm increases with time when $ZnFe_2O_4$-TiO_2 nanocomposites are irradiated by visible light. However, no PL peak at 425 nn is observed for $ZnFe_2O_4$-TiO_2 in the absence of visible light, clearly indicating the production of ·OH by $ZnFe_2O_4$-TiO_2 nanocomposites under visible light irradiation.

reaction with stable degradation efficiency of > 99% under visible light irradiation. Our results clearly demonstrate that the combination of low mass of $ZnFe_2O_4$ with anatase TiO_2 is a reliable green chemistry approach with great potential applications of utilizing visible light to decompose recalcitrant and emerging pollutants in water and wastewater treatments.

Acknowledgements

4. Conclusions

In this study, we have successfully fabricated a novel $ZnFe_2O_4$-TiO_2 nanocomposite with various mass loadings of 0.2–2 wt% $ZnFe_2O_4$ for the enhanced photocatalytic degradation of organic dyes under 465 nm visible light irradiation. The TEM images show that the average particle sizes of $ZnFe_2O_4$ and anatase TiO_2 nanoparticles are 8 – 9 nm. The optical property clearly indicates the possible electron transfer at the interface of $ZnFe_2O_4$ and anatase TiO_2 nanoparticles, resulting in the acceleration of photodegradation efficiency and rate of organic dyes under visible light irradiation. The photodegradation rate of organic dyes by 1 wt% $ZnFe_2O_4$-TiO_2 follows the order RhB > MR > MO. In addition, the 1 wt% $ZnFe_2O_4$-TiO_2 can retain its photocatalytic efficiency for at least 5 cycles of

Notes and references

1   W. Wu, C. Z. Jiang, V. A. L. Roy, Nanoscale, 2015, 7, 38-58.
2   M. A. Lazar, S. Varghese, S. S. Nair, Catalysts, 2012, 2, 572-601.
3   J. Y. Gan, X. H. Lu, Y. X. Tong, Nanoscale, 2014, 6, 7142-7164.
4   S. A. Ansari, M. H. Cho, Sci. Rep.,, 2016, 6, 25405.
5   R. Sedghi, F. Heidari, RSC Adv., 2016, 6, 49459-49468.
6   Y. Luo, Z. Lu, Y. Jiang, D. Wang, L. Yang, P. Huo, Z. Da, X. Bai, X. Xie, P. Yang, Chem. Eng. J., 2014, 240, 244-252.
7   C. Han, N. Zhang, Y.-J. Xu, Nano Today, 2016, 11, 351-372.
8   S. Liu, C. Han, Z. R. Tan, Y. -J. Xu, Mater. Horiz., 2016, 3, 270-282.
9   M. Q. Yang, Y. -J. Xu, Nanoscale Horiz., 2016, 1, 185-200.
10 R. A. Doong, S. M. Chang, C. W. Tsai, Appl. Catal. B: Environ., 2013, 129, 48-55.

ARTICLE

Journal Name

11 R. A. Doong, C. W. Tsai, J. Taiwan Inst. Chem. Eng. 2015, 57, 69-76.

12 Y. B. Liu, Q. F. Yao, X. J. Wu, T. K. Chen, Y. Ma, C. N. Ong, J. P. Xie, Nanoscale, 2016, 8, 10145-10151.

13 S. Semlali, T. Pigot, D. Flahaut, J. Allouche, S. Lacombe, L. Nicole, Appl. Catal. B: Environ., 2014, 150, 656-662.

14 P. Yu, S. S. Wang, H. H. Li, W. X. Li, Adv. Environ. Technol., 2013, 726-731, 673-676.

15 B. Sambandam, A. Surenjan, L. Philip, T. Pradeep, ACS Sustain. Chem. Eng., 2015, 3, 1321-1329.

16 P. Xu, T. Xu, J. Lu, S. M. Gao, N. S. Hosmane, B. B. Huang, Y. Dai, Y. B. Wang, Energ. Environ. Sci., 2010, 3, 1128-1134.

17 E. M. Samsudin, S. B. Abd Hamid, J. C. Juan, W. J. Basirun, G. Centi, Chem. Eng. J., 2015, 280, 330-343.

18 V. Stengl, S. Bakardjieva, N. Murafa, V. Houskova, K. Lang, Micropor. Mesopor. Mater., 2008, 110, 370-378.

19 M. T. Uddin, Y. Nicolas, C. Olivier, T. Toupance, M. M. Mueller, H. -J. Kleebe, K. Rachut, J. Ziegler, A. Klein, W. Jaegermann, J. Phys. Chem. C, 2013, 117, 22098-22110.

20 J. Shen, Y. Meng, G. Xin, Rare Metals, 2011, 30, 280-283.

21 Y. Xin, M. Gao, Y. Wang, D. Ma, Chem. Eng. J., 2014, 242, 162-169.

22 Y. Wang, Y. Z. Zheng, S. Q. Lu, X. Tao, Y. K. Che, J. F. Chen, ACS Appl. Mater. Interfaces, 2015, 7, 6093-6101.

23 D. L. Liao, C. A. Badour, B. Q. Liao, J. Photochem. Photobiol. A Chem., 2008, 194, 11-19.

24 M. Khatamian, M.S. Oskoui, M. Haghighi, M. Darbandi, Int. J. Energ. Res., 2014, 38, 1712-1726.

25 B. Wang, H. Zhang, X. -Y. Lu, J. Xuan, M. K. H. Leung, Chem. Eng. J., 2014, 253, 174-182.

26 P. Khemthong, P. Photai, N. Grisdanurak, Int. J. Hydrogen Energ., 2013, 38, 15992-16001.

27 L. F. Chiang, R. A. Doong, J. Hazard. Mater., 2014, 277, 84-92.

28 C. Santhosh, P. Kollu, S. Felix, V. Velmurugan, S. K. Jeong, A. N. Grace, RSC Adv., 2015, 5, 28965-28972.

29 I. L. Liakos, M. H. Abdellatif, C. Innocenti, A. Scarpellini, R. Carzino, V. Brunetti, S. Marras, R. Brescia, F. Drago, P. P. Pompa, Molecules, 2016, 21, 520-534.

30 M. Kooti, P. Kharazi, H. Motamedi, J. Mater. Sci. Technol., 2014, 30, 656-660.

31 H. Y. Zhu, R. Jiang, Y. Q. Fu, R. R. Li, J. Yao, S. T. Jiang, Appl. Surf. Sci., 2016, 369, 1-10.

32 A. Tadjarodi, M. Imani, M. Salehi, RSC Adv., 2015, 5, 56145-56156.

33 R. Dom, R. Subasri, K. Radha, P. H. Borse, Solid State Commun., 2011, 151, 470-473.

34 J. Q. Pan, X. Y. Li, Q. D. Zhao, D. K. Zhang, RSC Adv., 2015, 5, 51308-51317.

35 X. Y. Liu, H. W. Zheng, Y. Li, W. F. Zhang, J. Mater. Chem. C, 2013, 1, 329-337.

36 Y. J. Yao, Y. M. Cai, F. Lu, J. C. Qin, F. Y. Wei, C. Xu, S. B. Wang, Ind. Eng. Chem. Res., 2014, 53, 17294-17302.

37 W. Q. Zhang, M. Wang, W. J. Zhao, B. Q. Wang, Dalton Trans., 2013, 42, 15464-15474.

38 A. R. Upreti, Y. Li, N. Khadgi, S. Naraginti, C. Zhang, RSC Adv., 2016, 6, 32761-32769.

39 X. Zhu, F. Zhang, M. Wang, J. Ding, S. Sun, J. Bao, C. Gao, Appl. Surf. Sci., 2014, 319, 83-89.

40 M. Y. Wang, L. Sun, J. H. Cai, P. Huang, Y. F. Su and C. J. Lin, J. Mater. Chem. A, 2013, 1, 12082-12087.

41 Q. Q. Xu, J. T. Feng, L. C. Li, Q. S. Xiao and J. Wang, J. Alloy. Compd., 2015, 641, 110-118.

42 Y. J. Yao, J. C. Qin, H. Chen, F. Y. Wei, X. T. Liu, J. L. Wang and S. B. Wang, J. Hard. Mater., 2015, 291, 28-37.

43 G. X. Song, F. Xin and X. H. Yin, J. Colloid Interface Sci., 2015, 442, 60-66.

44 Z. H. Yuan and L. D. Zhang, J. Mater. Chem., 2001, 11, 1265-1268.

45 Y. Bu, Z. Chen, W. Li, Dalton Trans., 2013, 42, 16272-16275.

46 Y. Fu, X. Wang, Ind. Eng. Chem. Res., 2011, 50, 7210-7218.

47 M. K. Nowotny, P. Bogdanoff, T. Dittrich, S. Fiechter, A. Fujishima, H. Tributsch, Mater. Lett., 2010, 64, 928-930.

48 L. Kong, Z. Jiang, T. Xiao, L. Lu, M. O. Jones, P. P. Edwards, Chem. Commun., 2011, 47, 5512-5514.

49 Y. Hou, X. -Y. Li, Q. -D. Zhao, X. Quan, G. -H. Chen, Adv. Funct. Mater., 2010, 20, 2165-2174.

50 M. G. Mendez-Medrano, E. Kowalska, A. Lehoux, A. Herissan, B. Ohtani, D. Bahena, V. Briois, C. Colbeau-Justin, J. L. Rodriguez-Lopez, H. Remita, J. Phys. Chem. C, 2016, 120, 5143-5154.

51 R. Pandiyan, N. Delegan, A. Dirany, P. Drogui, M. A. El Khakani, J. Phys. Chem. C, 2016, 120, 631-638.

52 X. Li, Y. Hou, Q. Zhao, G. Chen, Langmuir, 2011, 27, 3113-3120.

53 S. A. Ansari, M. M. Khan, S. Kalathil, A. Nisar, J. Lee, M. H. Cho, Nanoscale, 2013, 5, 9238-9246.

54 C. Jin, B. Liu, Z. Lei, J. Sun, Nanoscale Res. Lett., 2015, 10, 1-9.

55 L. F. Chiang, R. A. Doong, Sep. Purif. Technol., 2015, 156, 1003-1010.

56 D. Nassoko, Y. -F. Li, H. Wang, J. -L. Li, Y. -Z. Li, Y. Yu, J. Alloy. Compd., 2012, 540, 228-235.

57 S. Pitchaimuthu, S. Rajalakshmi, N. Kannan, P. Velusamy, Desalin. Water Treat., 2014, 52, 3392-3402.

58 S. Zhang, J. Li, M. Zeng, G. Zhao, J. Xu, W. Hu, X. Wang, ACS Appl. Mater. Interfaces, 2013, 5, 12735-12743.

59 P. Zhou, J. G. Yu, M. Jaroniec, Adv. Mater. 2014, 26, 4920-4935.

60 W. -J. Ong, L. -L. Tan, S. -P. Chai, S. -T. Yong, Chem. Commun., 2015, 51, 858-861.

RSC Advances Accepted Manuscript